Expert Systems With Applications 255 (2024) 124656

Contents lists available at ScienceDirect

Expert Systems With Applications

journal homepage: www.elsevier.com/locate/eswa

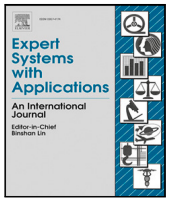

Accurate synthesis of sensor-to-machined-surface image generation in carbon fiber-reinforced plastic drilling

Jae Gyeong Choi [a], Dong Chan Kim [b], Miyoung Chung [c], Gyeongho Kim [a], Hyung Wook Park [b], Sunghoon Lim [a,d,e,*]

[a] Department of Industrial Engineering, Ulsan National Institute of Science and Technology, Ulsan, 44919, Republic of Korea
[b] Department of Mechanical Engineering, Ulsan National Institute of Science and Technology, Ulsan, 44919, Republic of Korea
[c] Montreal Neurological Institute, McGill University, 3801 Rue University, QC H3A 2B4, Canada
[d] Graduate School of Artificial Intelligence, Ulsan National Institute of Science and Technology, Ulsan, 44919, Republic of Korea
[e] Industry Intelligentization Institute, Ulsan National Institute of Science and Technology, Ulsan, 44919, Republic of Korea

ARTICLE INFO

Keywords:
Carbon fiber-reinforced plastic
Delamination prediction
Drilling process
Machined surface image generation
Sensor to image generation

ABSTRACT

Delamination is a prevalent issue in carbon fiber-reinforced plastic (CFRP) drilling, significantly compromising the mechanical properties of the material. Considering that delamination can impact the long-term durability of the final products, it is essential for operators to promptly identify it. This paper proposes a machined surface image generation model, called Sensor2Image, that employs time-series force sensor data as input and generates drilled-hole surface images as output. Sensor2Image first encodes the force sensor data into images using the Gramian angular field (GAF) method. Subsequently, it applies an image-to-image translation technique to generate the final machined surface images. The proposed model was trained and evaluated using experimental data gathered from drilling CFRP specimens under an industrial robot machining system. The results demonstrated the versatility of the proposed model for practical applications, regardless of the delamination factor. The proposed method offers significant advantages over existing methods through its intuitive visual representation approach. It facilitates the visual inspection of delamination while enabling surface quality analysis of the drilled hole and identification of defects or irregularities that may impact the mechanical properties of the material. The proposed approach can enhance the efficiency and reliability of industrial processes, particularly those involving complex delamination factors. It is a valuable tool for optimizing the CFRP drilling process and enhancing drilled-hole quality in a user-friendly manner.

1. Introduction

Carbon fiber-reinforced plastic (CFRP) is a widely used material in the aerospace and automotive industries owing to its exceptional strength-to-weight ratio and corrosion resistance (Chen et al., 2023). These qualities render CFRP ideal for high-demand applications, such as aircraft components and high-performance vehicles (Pérez-Salinas et al., 2023; Sun et al., 2021). However, the anisotropic nature of CFRP poses significant challenges in machining processes, particularly in drilling. This material is susceptible to various defects, including delamination, which can detrimentally affect the structural integrity and longevity of the final products (Xu et al., 2023). However, the challenges posed by CFRP drilling extend beyond the physical properties of the material. The high precision required for aerospace and automotive applications implies that even minor defects can significantly affect safety and performance (Ozkan et al., 2020). Moreover, the increasing complexity of designs necessitates more intricate drilling patterns, increasing the complexity of CFRP machining. This complexity further increases the risk of defects and necessitates advanced methods for monitoring and quality control during drilling process (Geier et al., 2023). Therefore, predicting delamination during CFRP drilling operations is crucial for enabling workers in taking appropriate measures, thereby enhancing production efficiency and ensuring the reliability of the final product.

Various methods have been employed to predict CFRP delamination during the drilling process. These include theoretical analysis, finite element (FE) simulation, and statistical approaches. Theoretical analysis involves the development of analytical mechanical models. For instance, Ismail et al. (2017) proposed an analytical thermo-mechanical model considering drill characteristics, such as chisel edge load and

* Corresponding author at: Department of Industrial Engineering, Ulsan National Institute of Science and Technology, Ulsan, 44919, Republic of Korea.
E-mail addresses: choil6043@unist.ac.kr (J.G. Choi), kdc9505@unist.ac.kr (D.C. Kim), miyoung.chung@mail.mcgill.ca (M. Chung), kkh0608@unist.ac.kr (G. Kim), hwpark@unist.ac.kr (H.W. Park), sunghoonlim@unist.ac.kr (S. Lim).

https://doi.org/10.1016/j.eswa.2024.124656
Received 10 January 2024; Received in revised form 18 June 2024; Accepted 28 June 2024
Available online 6 July 2024

Nomenclature

Acronyms

cGAN	conditional Generative Adversarial Network
GAF	Gramian Angular Field
GASF	Gramian Angular Summation Field
GADF	Gramian Angular Difference Field
ReLU	Rectified Linear Unit
LS	Least Square
BCE	Binary Cross Entropy
PSNR	Peak Signal-to-Noise Ratio
SSIM	Structural Similarity Index Measure
MSE	Mean Squared Error
MAE	Mean Absolute Error
MAPE	Mean Absolute Percentage Error
S2I	Sensor2Image
GS-S2I	Gramian Angular Summation Field-based Sensor2Image
GD-S2I	Gramian Angular Difference Field-based Sensor2Image

Symbols

G	Generator
D	Discriminator
F_d	One-dimensional conventional delamination factor
F_a	Two-dimensional delamination factor
F_{da}	Adjusted delamination factor
D_{max}	Maximum diameter of the damage zone
D_0	Hole diameter
A_d	Quotient of the delaminated area
A_{norm}	Hole area
A_{max}	Area associated with the maximum diameter of the damage zone
N	Number of samples
$\mathcal{D}$	Sensor-image pairs
$\mathcal{D}'$	Aligned image pairs
s_i	Time-series sensory data
x_i	Image transformed from sensory data s_i
y_i	Ground truth machined surface image
$\hat{y}_i$	Generated machined surface image
d_i	Delamination factor on the ground truth image
$\hat{d}_i$	Delamination factor on the generated image

point angle, to predict the critical thrust force and feed rate. Girot et al. (2017) established correlations between cutting forces and delamination, focusing on the loading on the drill cutting edge. Further, Su et al. (2019) developed an analytical model based on the classical bending theory of beams and linear elastic fracture mechanics to predict the exit-delamination morphology of CFRP drilling. FE simulation has been extensively used in machining to create computational models that predict the mechanical behavior of workpieces. Feito et al. (2014) employed FE analysis to anticipate the extent and occurrence of delamination during simulated drilling processes. Sugita et al. (2019) utilized a high-fidelity FE model to simulate the drilling process and predict delamination and burr formation in CFRP. The insights gained from their study can be used to design drill tools that minimize defects during CFRP drilling. Similarly, Seo et al. (2021) used cohesive zone models to predict the delamination factor while considering cutting and backup plate conditions. Further, several statistical approaches have been applied to predict delamination in CFRP drilling. Davim and Reis (2003) established correlations between cutting parameters and feed rate with a delamination factor using multiple linear regression. Krishnamoorthy et al. (2015) developed a quadratic mathematical model to predict the one-dimensional delamination factor. They employed analysis of variance (ANOVA) to statistically evaluate the model's adequacy and found a strong correlation between the input parameters and the output response. In addition, Zhang and Xu (2020) achieved accurate and stable prediction performance by using a Gaussian process regression model for predicting the delamination factor during drilling. They further utilized the Taguchi method to identify the statistical correlations between process parameters and the final quality of the workpiece.

The adoption of data-driven machine learning and deep learning techniques in the manufacturing sector has garnered significant attention in recent years (Kim et al., 2023a, 2023b). Numerous studies have focused on data-driven approaches that use sensory data collected during the drilling process to predict hole quality (Choi et al., 2024; Norcahyo et al., 2019; Volety & Mani, 2023; Yi et al., 2019). These methods typically involve predicting delamination assessment factors, such as the conventional one-dimensional (F_d), two-dimensional (F_a), and adjusted (F_{da}) delamination factors. These factors were derived from image-processing techniques applied to hole surfaces acquired using optical microscopes. Although these approaches have shown promise, their ability to simultaneously predict multiple delamination factors is limited. This limitation poses a significant challenge because the specific factors required for a given operation may vary depending on its purpose. Previous studies predominantly predicted a single delamination factor (e.g., F_d) at a time, lacking simultaneous predictions of other relevant factors (e.g., F_a or F_{da}) despite their significance. Even when multiple delamination factors were simultaneously predicted, the number of factors considered was limited. This makes the predictions infeasible for application across all drilling processes. This gap in predictive capabilities highlights the necessity for a more comprehensive and versatile model that can adapt to the varied demands of drilling process and deliver multifaceted predictions.

A comprehensive approach encompassing machine learning and suitable preprocessing techniques is necessary to address this challenge in CFRP drilling. The application of machine learning to time-series sensor data in the manufacturing industry has been extensively researched. A key component of this approach involves preprocessing methods critical for enhancing data quality before their application in machine-learning models. These methods include statistical feature extraction (Sen et al., 2023), time-frequency domain analysis (Liu et al., 2020), and dimensionality reduction (Nadir et al., 2020). Image transformation has been employed in several applications to enhance the analysis and interpretation of time-series sensor data. Through the conversion of sensor data into visual representations, these studies leverage the advanced feature extraction and analysis capabilities of machine-learning algorithms, resulting in enhanced performance and effectiveness across diverse tasks. For example, Ciecieląg et al. (2021) utilized image-based techniques to detect delamination in composite materials, including CFRP, during the drilling process. They converted the time series cutting force data, recorded throughout the drilling operation, into recurrence plot (RP) images. Chen et al. (2022) introduced an integrated learning method based on the gramian angular field (GAF) and optimal feature channel adaptive selection for rolling bearing fault diagnosis, demonstrating an improved classification performance compared with state-of-the-art approaches. These studies highlight the growing interest in converting sensor data into images for enhanced analysis and diagnosis of defect (Jiang & Chen, 2023; Li et al., 2024; Wang et al., 2023).

Image-to-image translation, a concept gaining prominence in computer vision, enables the transformation of input images into desired output images using deep-learning techniques. Image-to-image translation has been increasingly employed in the manufacturing industry for quality control, predictive maintenance, virtual prototyping, and enhanced process visualization (Adachi et al., 2020; Déau et al., 2023; Huang et al., 2021). Isola et al. (2017) presented a significant advancement in this approach. They introduced the pix2pix model, a foundational approach for paired image-to-image translation tasks. This model is anchored in a conditional generative adversarial network (cGAN) framework, enabling the generation of realistic images from input–output pairs. Subsequent research has led to a series of innovative developments based on this foundation. Among these is the pix2pixHD model introduced by Park et al. (2019), which extends the capabilities of the original pix2pix framework. Pix2pixHD enhances the photorealism and resolution of generated images, supporting high-definition outputs up to 2048 × 1024 resolution. This advancement significantly improves the visual quality and applicability of the image translation in more demanding scenarios. Another notable contribution is the SPADE, proposed by Wang et al. (2018). This model integrates spatially-adaptive normalization layers, significantly enhancing the quality of synthesized images. Its approach excels at handling diverse and complex image contents, making it a versatile tool in image-to-image translation tasks. Further contributing to the field is ASAPNet by Shaham et al. (2021), distinguished as a lightweight yet efficient network. It is specifically designed to facilitate rapid and high-resolution image-to-image translation tasks, addressing speed and efficiency requirements in real-time and resource-constrained applications.

This paper proposes a novel sensor-to-image generation model called Sensor2Image, which translates force sensor data into machined surface images during the CFRP drilling process. In contrast to previous studies that focused solely on predicting a single delamination factor, the proposed approach generates complete surface images, capturing the intricate details and characteristics of the drilled holes. This enables extraction and analysis of multiple factors, addressing the diverse requirements and variations encountered in drilling operations. By generating images rather than estimating a predefined delamination value, the proposed approach enhances insights into the drilling process, facilitates visual inspection, and analyzes potential delamination areas.

The primary contributions of this work to the literature are as follows:

1. This work introduces a novel hole surface image generation model that utilizes force sensor data, employing an image-to-image translation approach, to effectively predict the delamination potential of drilled CFRP surfaces. This advancement improves the delamination prediction accuracy and adapts flexibly to diverse drilling process requirements.
2. The proposed model provides an intuitive and user-friendly approach for delamination inspection by leveraging the generated images of the drilled-hole surfaces. This method significantly simplifies delamination assessment while delivering superior performance.

The remainder of this paper is organized as follows. Section 2 outlines the proposed method, including the preprocessing techniques, model architecture, and theoretical descriptions. Section 3 presents the experimental settings, including the data collection process. Section 4 quantitatively and qualitatively evaluates the performance of the proposed model and compares it with existing methods. Finally, Section 5 concludes the paper by summarizing the contributions of this work and highlighting future research directions.

2. Methods

This work aims to develop a method for generating machined surface images of CFRP holes based on time-series force sensor data collected during the drilling process. To achieve this goal, the proposed Sensor2Image is divided into two stages. The first stage involves transforming the sensory data into image representations. The second stage uses an image-to-image translation technique to generate the final output image of the machined-hole surface. Specifically, the time-series force sensor data are transformed into an image representation using polar encoding transformation, which is then fed into the image-to-image translation model to generate the machined surface image. The transformed input data are used to train the model to generate the desired output image. Fig. 1 shows the Sensor2Image structure.

2.1. Sensor2Image

Using the sensor-image data pairs $D = \{s_i, y_i\}_{i=1}^{N}$, where s_i is a force sensor and y_i is the machined surface image, the model aims to map a source image transformed from the sensor data and a machined surface image. This model is based on the pix2pix framework and employs an adversarial learning approach. During training, the model aims to minimize adversarial loss and L_1 loss between the source and target images. By optimizing the combined loss function, Sensor2Image learns to generate source images that accurately represent the corresponding machined surface images.

2.2. Sensory data to image transformation

The input for Sensor2Image is prepared using the GAF proposed by Wang and Oates (2015). GAF is used to encode time-series sensor data into images that preserve temporal dependency. This framework transforms a time series into a polar coordinate system, where each point in the time-series signal is mapped to a point on a unit circle. The outer product of each pair of points on the circle is calculated, followed by the cosine of the resulting product summation.

The resulting matrix is used for image representation. The time-series data $S = \{s_i\}_{i=1}^{T}$ then undergoes a min–max scaling transformation (Patro & Sahu, 2015) to ensure that all values are within the range of [−1, 1].

$$\tilde{s}_1^i = \frac{\left(s_i - \max(S)\right) + \left(s_i - \min(S)\right)}{\max(S) - \min(S)} \tag{1}$$

The rescaled time series is encoded as the angular cosine and the timestamp as the radius, thereby preserving the absolute temporal relations in the polar coordinate system (Wang et al., 2022), as calculated using (2). The corresponding values warp between different angular points on the spanning circles as time increases. This encoding map produces a unique result in a polar coordinate system with a unique inverse map given a time series.

$$\begin{cases} \phi = \arccos\left(\tilde{s}_i\right), -1 \le \tilde{s}_i \le 1, \tilde{s}_i \in \tilde{S} \\ r_i = \frac{t_i}{N}, t_i \in \mathbb{N} \end{cases}, \tag{2}$$

where t_i indicates the time stamp and N is used to control the span of the polar coordinate system.

GAF can be computed using two different Gramian matrix calculation methods: Gramian Angular Summation Field (GASF) and Gramian Angular Difference Field (GADF). The GASF is derived from the GAF representation by taking the sum of each pair of values in the GAF matrix, resulting in a new matrix with the same dimensions as the GAF matrix. The GASF matrix X_{GASF} represents the summation of the angles between each pair of time points in the time series.

$$\begin{aligned} X_{GASF} &= \begin{bmatrix} \cos\left(\phi_1 + \phi_1\right) & \cdots & \cos\left(\phi_1 + \phi_n\right) \\ \cos\left(\phi_2 + \phi_1\right) & \cdots & \cos\left(\phi_2 + \phi_n\right) \\ \vdots & \ddots & \vdots \\ \cos\left(\phi_n + \phi_1\right) & \cdots & \cos\left(\phi_n + \phi_n\right) \end{bmatrix} \\ &= \tilde{S}' \cdot \tilde{S} - \sqrt{I - \tilde{S}'^2} \cdot \sqrt{I - \tilde{S}^2} \end{aligned} \tag{3}$$

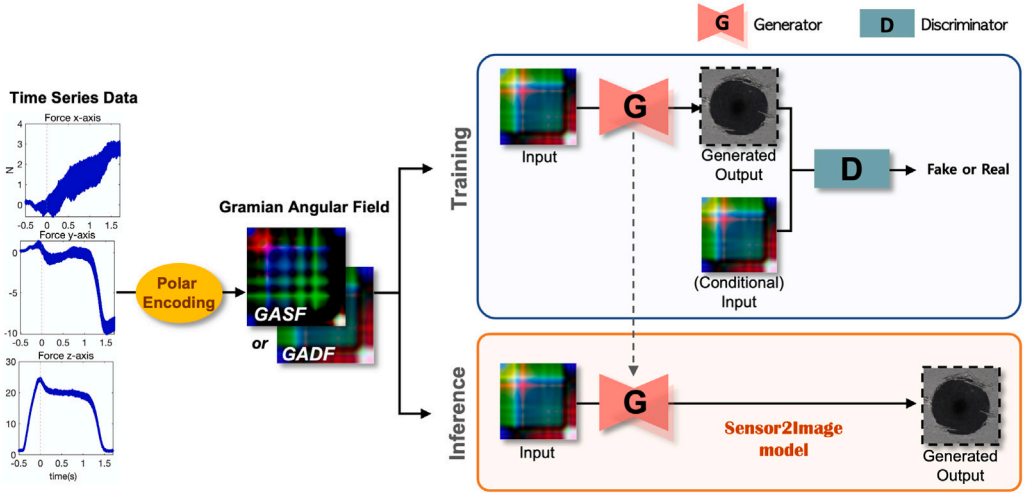

Fig. 1. Overall structure of Sensor2Image.

where I denotes the unit vector. After transformation to the polar coordinate system, the time series at each time step is considered as a one-dimensional (1D) metric space. However, GADF takes the difference between each pair of values in the GAF matrix, resulting in a new matrix with the same dimensions as the GAF matrix. The GADF matrix X_{GADF} represents the difference in angles between each pair of time points in the time series.

$$X_{GADF} = \begin{bmatrix} \sin(\phi_1 - \phi_1) & \cdots & \sin(\phi_1 - \phi_n) \\ \sin(\phi_2 - \phi_1) & \cdots & \sin(\phi_2 - \phi_n) \\ \vdots & \ddots & \vdots \\ \sin(\phi_n - \phi_1) & \cdots & \sin(\phi_n - \varnothing_n) \end{bmatrix} = \sqrt{I - \tilde{S}'^2} \cdot \tilde{S} - \tilde{S}' \cdot \sqrt{I - \tilde{S}^2} \tag{4}$$

2.3. Image-to-image translation for generating machined surfaces

The proposed Sensor2Image is an adaptation of the pix2pix scheme specifically designed to address the challenges of generating machined surface images during the CFRP drilling process. Pix2pix uses the cGAN framework, which involves a generator and discriminator. The generator produces realistic images from the GAF image, which contains the temporal dependency of the force sensor data. The discriminator distinguishes between real and generated images. This adversarial training process encourages the generator to generate high-quality images that are indistinguishable from the real images. By leveraging image-to-image translation capabilities, the proposed model transforms specific aspects of the input image to generate the desired machined surface image. Image-to-image translation tasks can change one aspect of a given image into another.

Mapping is learned using a set of training data, which may comprise aligned image pairs $D' = \{x_i, y_i\}_{i=1}^{N}$, where an image translated from sensory data $x_j \in X$, a machined surface image $y_j \in Y$, and N is the number of samples. The training set is resized and cropped to 256×256 pixels for a clear center-of-the-hole surface, the same size as that of the source image. The images are then normalized to the $[-1, 1]$ range.

The convolutional PatchGAN serves as a discriminator that efficiently extracts receptive fields from the CNN architecture, allowing for flexibility in image size and detailed feature discernment using patches. This discriminator determines whether each image patch is real or fake, as shown in Fig. 2. Each block in the discriminator comprises convolutional layers, batch normalization, and a leaky rectified linear unit (ReLU).

In this work, a notable modification to the standard pix2pix model is the incorporation of the least-squares loss function for the discriminator, diverging from the traditional binary cross entropy (BCE)

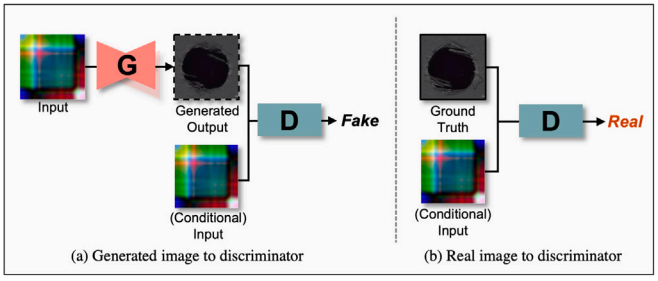

Fig. 2. Discriminator training. The discriminator learns to distinguish between generated and real machined surface images, conditioned on the input GAF image. (a) The generator produces a machined surface image based on the input GAF image, and the discriminator classifies it as fake. (b) The discriminator classifies the ground truth machined surface image as real, given the corresponding input GAF image. Through this process, the discriminator is trained to distinguish between generated and real images, providing feedback to enhance the generator's output quality.

loss. Inspired by the approach proposed by Mao et al. (2017), this adaptation promotes a stable training process by addressing vanishing gradient issues and encouraging smoother convergence. This reduces the likelihood of mode collapse. In addition, this function provides a more informative measure of the discriminator confidence. This results in an improved discrimination capability and higher-quality generated samples. By minimizing the distributional divergence, the least squares (LS) loss function aligns with the broader objective of generating more realistic outputs.

$$L_D = \frac{1}{2}\mathbb{E}_{x \sim p_{\text{data}}}\left[(D(x) - 1)^2\right] + \frac{1}{2}\mathbb{E}_{z \sim p_z}\left[D(G(z))^2\right] \tag{5}$$

The pix2pix generator is a modified U-Net comprising an encoder and decoder with downsampling and upsampling blocks, respectively. Each block in the encoder comprises convolutional layers, batch normalization, and leaky ReLU. Each block in the decoder comprises a transposed convolution for upsampling, batch normalization, dropout, and ReLU for activation. Skip connections are incorporated in the early stages to convey information between the encoder and decoder. This enables the model to preserve fine-grained information by facilitating the passage of relevant information from the encoder to the decoder. Employing this architectural approach proved effective in preserving structural coherence in the generated images. Fig. 3 shows the detailed architectures of the generator and discriminator.

The generator is updated using a loss function that merges adversarial and L_1 losses. The adversarial loss ensures that the generator model can produce images that appear authentic within the target

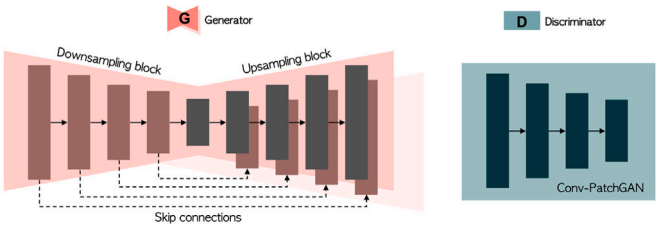

Fig. 3. The architecture of the generator and the discriminator of Sensor2Image.

domain. The L_1 loss serves as a regularization mechanism, enabling the generator to yield images that plausibly translate the source image.

$$\mathcal{L}_{cGAN}(G, D) = \mathbb{E}_{x,y}[\log D(x, y)] + \mathbb{E}_{x,z}[\log(1 - D(x, G(x, z)))] \tag{6}$$

$$\mathcal{L}_{L_1}(G) = \mathbb{E}_{x,y,z}\left[\|y - G(x, z)\|_1\right] \tag{7}$$

A weight hyperparameter, λ, adjusts the balance between the L_1 loss and adversarial losses. Adjusting λ values involves a trade-off between image quality and fidelity. Decreasing the λ applied to the L_1 loss in the generator loss causes the generated outputs to exhibit more diversity and creativity while potentially introducing more noise and inconsistencies. Conversely, increasing the λ weight places a stronger emphasis on exact alignment with the ground truth, resulting in generated images that closely match the target and reproduce fine details more accurately.

$$G^* = \arg\min_G \max_D \mathcal{L}_{cGAN}(G, D) + \lambda \mathcal{L}_{L_1}(G) \tag{8}$$

3. Experiment

3.1. Experimental setup

The experiment used a robotic arm with up to six axes connected to a spindle (HSD MT1055) using a rigid bracket. The machining conditions and paths were set using the commercial software Master Cam and Robot Master, respectively. A feed rate of 0.02 mm/rev and rotational speed of 6000 RPM were used to ensure that the cutting force did not exceed the 7 kg payload and cause severe vibrations. Fig. 4 shows the experimental setup. The cutting force was measured using a dynamometer at a sampling rate of 2000 Hz. The cutting force sensor data used in this work was subjected to preprocessing, as described in Choi et al. (2024). The data was processed using a 5 Hz low-pass filter and a moving average technique with a window size of 0.5 s to eliminate noise. This reduced the influence of slight vibrations in robot machining. Further, its charge amplifier and data acquisition system measured and recorded the cutting force, whereas a data logger (DAQ9234; LabVIEW National Instruments, Inc.) performed other measurements. A total of 500 holes, each with a diameter of 2 mm, were drilled using diamond-coated carbide tools. The dataset comprised 500 holes, distributed across five plates with 100 holes per plate. A single tool was used to drill each plate, yielding 100 holes per tool to minimize wear-induced experimental error. The CFRP used was a 3 mm thick unidirectional material made of 11 fabric plies of SK SKYFLEX USN300B prepregs, cured in an autoclave for 90 min at 125 °C under 5 bar. Table 1 lists the detailed CFRP properties. The optical images of the machined surfaces were obtained using a VHX-7000 microscope (Keyence).

3.2. Implementation details

The model was trained on a single NVIDIA RTX A6000 for 200 epochs. The batch size was set to 1, executed for three runs to accommodate the potential variability resulting from random initialization. The dataset was divided into training and test sets in an 8:2 ratio.

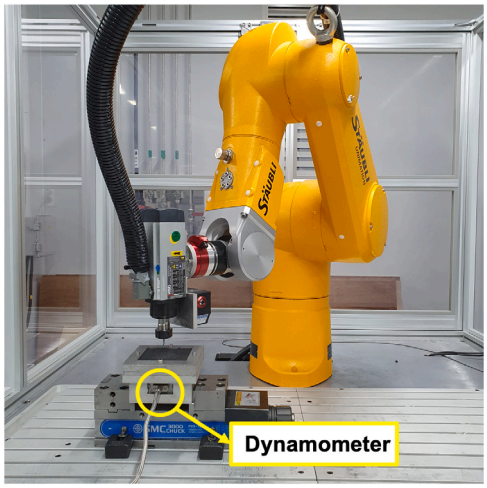

Fig. 4. Experimental setup for CFRP drilling using a robotic machining system.

Table 1
Experimental setting and CFRP material properties.

Experimental setting	
Parameter	Condition
Feed (mm/rev)	0.02
Rotating speed (RPM)	6000
Diameter of tool (mm)	2
CFRP thickness (mm)	3
Cutting tool	Diamond-coated carbide tool (Union tool)
Industrial robot	Staubli TX90
Spindle	HSD MT1055
Dynamometer	Kistler 9256C
Data logger	DAQ9234; LabVIEW National Instruments, Inc
CFRP material properties	
Property	Value
Fiber content (%)	67
Volume fraction of fiber (Vf) (%)	57
Young's modulus, E1 (GPa)	138
Young's modulus, E2, E3 (GPa)	8.02
Shear strength, τ_1 (MPa)	89
Shear strength, τ_2 (MPa)	63
Poisson's ratio, γ_{13}	0.31
Glass transition temperature (°C)	126
Decomposition temperature (°C)	405

The Adam optimizer with a learning rate $2e^{-4}$ and $\beta = 0.5$ was used for the generator and discriminator networks. Tables 2 and 3 list the averages and standard deviations of the results from these iterations, respectively.

4. Result

4.1. Quantitative analysis

Quantitative metrics were employed to measure the performance and effectiveness of Sensor2Image. A comparative analysis of the results is presented, considering cases with and without applying the modified discriminator loss function and optimal λ value determined through grid search. Furthermore, the delamination prediction performances of various machine-learning models were comparatively analyzed. This analysis provides insights into the effectiveness of Sensor2Image compared with alternative approaches. Considering multiple metrics and benchmarking against other models ensured a robust evaluation of the performance and effectiveness of the proposed approach.

Table 2
Quantitative evaluation of Sensor2Image configurations using quality assessment scores.

Loss	λ	GS-S2I		GD-S2I	
		PSNR (↑)	SSIM (↑)	PSNR (↑)	SSIM (↑)
BCE	40	21.92 ± 0.98	0.50 ± 0.02	21.97 ± 1.05	0.51 ± 0.02
	60	21.90 ± 1.05	0.51 ± 0.02	21.92 ± 1.07	0.51 ± 0.02
	80	22.67 ± 0.07	0.56 ± 0.04	22.27 ± 0.15	0.55 ± 0.00
	100	22.26 ± 0.03	0.51 ± 0.00	22.16 ± 0.23	0.53 ± 0.07
LS	40	21.96 ± 0.99	0.50 ± 0.02	21.96 ± 1.04	0.50 ± 0.02
	60	21.94 ± 0.97	0.51 ± 0.02	21.91 ± 1.05	0.50 ± 0.02
	80	**23.67 ± 0.30**	**0.60 ± 0.01**	**22.74 ± 0.07**	**0.61 ± 0.01**
	100	22.31 ± 0.23	0.54 ± 0.03	22.27 ± 0.33	0.55 ± 0.03

4.1.1. Image quality

The peak signal-to-noise ratio (PSNR) and structural similarity index measure (SSIM) (Wang et al., 2004) are widely used qualitative metrics in evaluating generated images.

The PSNR is used for assessing the quality of reconstructed or generated images. It quantifies the difference between the reference image and generated image in terms of the mean squared error (MSE). A higher PSNR generally indicates better performance, with the generated image being closer to the reference image in terms of pixel-wise differences.

$$\mathrm{PSNR} = 10\log_{10}\left(\frac{\mathrm{MAX}_{\hat{Y}}^2}{\mathrm{MSE}(\hat{Y}, Y)}\right) \tag{9}$$

where

$$\mathrm{MSE}(\hat{Y}, Y) = \frac{1}{mn}\sum_{i=0}^{m-1}\sum_{j=0}^{n-1}[Y(i,j) - \hat{Y}(i,j)]^2 \tag{10}$$

$\hat{Y}$ refers to the generated image, Y corresponds to the ground-truth image, and $\mathrm{MAX}_{\hat{Y}}^2$ denotes the maximum pixel value of the generated image, with m and n representing the height and the width of the image, respectively.

By contrast, the SSIM is a more sophisticated metric that considers structural, luminance, and contrast information in images. This provides a better indication of perceived visual quality. The SSIM tends to correlate better with the human perception of image quality. It ranges from −1 to 1, with a value of 1 indicating a perfect match between the reference and generated images.

$$\mathrm{SSIM}(\hat{y}, y) = \frac{\left(2\mu_{\hat{y}}\mu_y + c_1\right)\left(2\sigma_{\hat{y}y} + c_2\right)}{\left(\mu_{\hat{y}}^2 + \mu_y^2 + c_1\right)\left(\sigma_{\hat{y}}^2 + \sigma_y^2 + c_2\right)} \tag{11}$$

where $c_1 = \left(k_1 L\right)^2$ and $c_2 = \left(k_2 L\right)^2$ are variables used to stabilize the division with a weak denominator, and L is the dynamic range of the pixel values (usually $2^{\#\text{bits per pixel}} - 1$). μ represents the pixel sample mean, σ^2 denotes the variance, and $\sigma_{\hat{y}y}$ represents the covariance between the generated and ground-truth images.

In the original pix2pix model, the discriminator used the BCE loss function, and a λ value of 100 was used in (8). However, this work deviated from the original configuration and explored different options. Specifically, it compared the performance with the LS loss function while varying the λ value over a range of 40, 60, 80, and 100, as presented in Table 2. Two variants of Sensor2Image, namely, GS-S2I and GD-S2I, were quantitatively evaluated. These variants were derived from different image-transformation techniques applied to the sensor data. GS-S2I and GD-S2I represent GASF- and GADF-based Sensor2Image, respectively. This evaluation aimed to validate the impact of the choice of loss function on overall performance of the model and determine the optimal λ value. The range of λ values evaluated was 40, 60, 80, and 100.

Among the evaluated configurations, GS-S2I with an LS loss and a λ value of 80 achieved the highest PSNR score of 23.67 ± 0.30, indicating more accurate image reconstruction with the minimal distortion. By contrast, GD-S2I with an LS loss and a λ value of 80 achieved the highest SSIM score of 0.61 ± 0.01, indicating better preservation of structural and textural similarities between the generated and target images. Across the range of λ values of 40–100, the configuration with a λ value of 80 consistently exhibited superior performance compared to other settings. This value helped achieve a favorable balance between image quality and fidelity to the ground truth.

These results highlight the effectiveness of the LS loss function and an appropriate λ value in improving image quality and similarity in GS-S2I and GD-S2I. The LS loss function facilitates smoother gradients and improves convergence during training, resulting in pixel-wise accuracy and reduced image distortion. In addition, lowering the λ value to 80 results in more visually appealing and realistic generated images. Nonetheless, a balance is necessary because lowering the λ value excessively may introduce minor distortions in terms of pixel-wise similarity to the target image.

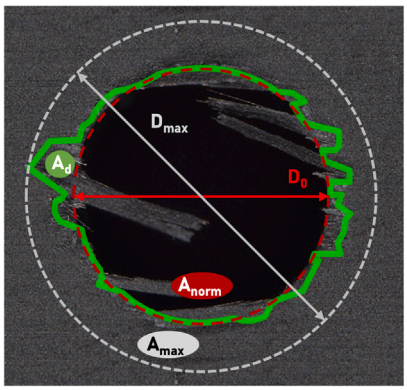

Fig. 5. Hole delamination assessment.

4.1.2. Retrieving delamination factors

Various delamination factors were computed to assess the quality of the generated image in relation to the ground-truth images and present the corresponding errors. This analysis validated the applicability of the proposed method to CFRP processes regardless of the delamination factor. Three factors were used for the evaluation: F_d, F_a, and F_{da}. These factors were measured using the distance or area from the machined surface hole, as shown in Fig. 5, calculated using (12) to (14).

$$F_d = \frac{D_{\max}}{D_0} \tag{12}$$

$$F_a = \left(\frac{A_d}{A_{norm}}\right)\% \tag{13}$$

$$F_{da} = F_d + \frac{A_d}{\left(A_{\max} - A_{norm}\right)}\left(F_d^2 - F_d\right) \tag{14}$$

Fig. 6 shows the image-processing steps to extract these factors from the ground-truth and generated images of a CFRP drilled-hole surface. These steps involve converting the image to grayscale, applying a Gaussian blur filter, contouring, and determining the maximum convex hull area. These steps help reduce noise, identify object boundaries, and obtain an objective measure of the size and shape of the drilled hole.

To validate the effectiveness of the proposed Sensor2Image, its performance was compared with those of various machine-learning models. These models utilize the statistical characteristics of raw force sensor values as inputs and extract nine time-domain features (minimum, maximum, peak-to-peak, median, root mean square (RMS), mean value, rectified mean value, variance, and standard deviation) as inputs, as suggested by Cui et al. (2021). The errors of each factor between the ground-truth and generated images were quantified using

Table 3
Quantitative analysis of delamination factors using error metrics.

	MAPE			MAE ($\times 10^{-2}$)		
	F_d	F_a	F_{da}	F_d	F_a	F_{da}
Linear	4.27 ± 0.06	23.46 ± 1.77	4.99 ± 0.03	5.15 ± 0.01	2.61 ± 0.01	6.52 ± 0.04
Ridge	4.22 ± 0.02	23.23 ± 0.21	4.98 ± 0.03	5.15 ± 0.01	**2.59 ± 0.01**	6.49 ± 0.01
Lasso	4.24 ± 0.02	22.72 ± 1.78	5.05 ± 0.01	5.21 ± 0.09	2.74 ± 0.00	6.54 ± 0.01
Decision Tree	5.39 ± 0.34	30.72 ± 0.96	6.06 ± 0.61	6.58 ± 0.49	3.72 ± 0.03	7.62 ± 0.18
Random Forest	4.41 ± 0.04	23.15 ± 1.87	5.18 ± 0.07	5.51 ± 0.03	2.67 ± 0.03	6.76 ± 0.08
Extra Trees	4.56 ± 0.05	23.59 ± 2.25	5.42 ± 0.10	5.54 ± 0.01	2.68 ± 0.03	7.02 ± 0.04
KNN	4.30 ± 0.02	23.78 ± 1.61	5.18 ± 0.01	5.30 ± 0.02	2.84 ± 0.01	6.68 ± 0.02
Elastic Net	4.24 ± 0.02	23.06 ± 1.29	5.04 ± 0.01	5.22 ± 0.09	2.73 ± 0.00	6.54 ± 0.01
AdaBoost	5.48 ± 0.05	23.11 ± 1.63	6.18 ± 0.18	6.55 ± 0.13	2.91 ± 0.02	7.69 ± 0.33
XGBoost	4.67 ± 0.15	23.38 ± 0.93	5.27 ± 0.04	5.51 ± 0.14	2.91 ± 0.12	6.87 ± 0.16
Gradient Boosting	4.17 ± 0.07	23.04 ± 0.66	5.08 ± 0.05	5.19 ± 0.08	2.65 ± 0.04	6.53 ± 0.06
LightGBM	4.59 ± 0.04	23.52 ± 0.15	5.53 ± 0.08	5.60 ± 0.02	2.85 ± 0.04	7.12 ± 0.10
pix2pixHD (Park et al., 2019)	3.95 ± 0.01	23.19 ± 2.69	4.93 ± 0.20	5.01 ± 0.01	3.40 ± 0.48	6.66 ± 0.28
SPADE (Wang et al., 2018)	4.19 ± 0.31	44.09 ± 4.66	6.10 ± 0.63	5.26 ± 0.40	5.84 ± 0.72	8.07 ± 0.86
ASAPNet (Shaham et al., 2021)	4.32 ± 0.56	36.06 ± 10.39	5.81 ± 1.09	5.33 ± 0.64	4.33 ± 1.12	7.52 ± 1.30
GS-S2I*	**3.57 ± 0.05**	**21.57 ± 0.60**	**4.36 ± 0.07**	**4.52 ± 0.07**	2.82 ± 0.17	**5.86 ± 0.09**
GD-S2I*	3.77 ± 0.06	23.77 ± 0.31	4.71 ± 0.12	4.76 ± 0.07	3.09 ± 0.09	6.34 ± 0.17

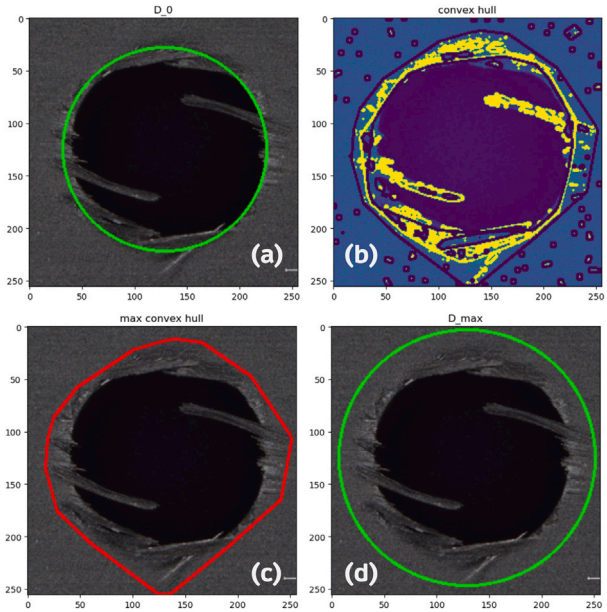

Fig. 6. Preprocessing steps for assessing hole delamination: (a) creating a circle for the drilled hole, (b) visualizing the convex hull of contours by applying Gaussian blur and filtering, (c) determining the maximum area of the convex hull, and (d) drawing a circle with a diameter equal to the maximum diameter of the defect.

the mean absolute percentage error (MAPE) and mean absolute error (MAE), calculated using (15) and (16).

$$\mathrm{MAPE} = \sum_{i=1}^{N} \left| \frac{\mathrm{d}_i - \hat{\mathrm{d}}_i}{\mathrm{d}_i} \right| \times \frac{100}{N}\% \tag{15}$$

$$\mathrm{MAE} = \frac{1}{N} \sum_{i=1}^{N} \left| \mathrm{d}_i - \hat{\mathrm{d}}_i \right| \tag{16}$$

where d_i and $\hat{\mathrm{d}}_i$ represent the delamination factors in the ground-truth and generated images, respectively.

Table 3 provides a quantitative analysis of the delamination factors using these error metrics. MAE is expressed in units of 10^{-2}. The comparison included various machine-learning models, including linear-, tree-, boosting-, and clustering-based models, each focusing on predicting a single delamination factor. These models were evaluated based on their performance in predicting the three delamination factors: F_d, F_a, and F_{da}. The values in bold in the table indicate the lowest error values for each delamination factor, highlighting the best model performance. The models marked with an asterisk, GS-S2I* and GD-S2I*, represent the two Sensor2Image models trained based on the LS loss function and a λ value of 80, determined as the optimal configuration on the results from Table 2.

The results demonstrated that the proposed approaches, GS-S2I* and GD-S2I*, exhibited superior performance in terms of MAPE and MAE for most delamination factors compared with the other models. However, the proposed approaches have room for improvement in predicting F_a on the generated images, as evidenced by their MAE values. This may be because F_d considers only the maximum delamination length, whereas F_a requires a 360° assessment of the overall delamination area. Therefore, generating more sophisticated machined-hole surface images is necessary for a more accurate F_a prediction. Enhancements in the F_a performance could potentially improve the F_{da} performance owing to the influence of F_d and F_a.

Despite their relatively higher MAE values for F_a, the GS-S2I* and GD-S2I* models offer the distinct advantage of simultaneously predicting all delamination factors. This distinguishes them from traditional machine-learning models, which typically focus on predicting a single delamination factor at a time. GS-S2I* and GD-S2I*, which generate machined-hole surface images, exhibit comparable or even superior prediction performance compared with these single-factor models. They can simultaneously estimate various factors by extracting relevant information from the generated image. This flexibility allows the models to have wide applicability because they are not limited to specific delamination factors. These models can adapt to various situations where different delamination factors may be considered.

4.1.3. Comparison with other baseline approaches

A comparative analysis was conducted to assess the performance of the proposed baseline model against existing literature on supervised image-to-image translation with a single-model output. The proposed baseline model is described in Section 2.3. The other baselines selected for comparison were pix2pixHD (Park et al., 2019), SPADE (Wang et al., 2018), and ASAPNet (Shaham et al., 2021).

Table 3 presents comparative results of the predictive performance of delamination factors. In addition, Table 4 compares the quality assessment metrics for images generated from the GASF and GADF representations by employing various baseline models. An assessment of the images shown in Fig. 7 revealed that the existing models were not the most suitable choices for the baseline. Pix2pixHD primarily focuses on generating high-resolution images, SPADE focuses on incorporating style information, and ASAPNet prioritizes rapid image translations. While these characteristics are valuable for specific applications, they are not highly relevant to the task considered, which involves using

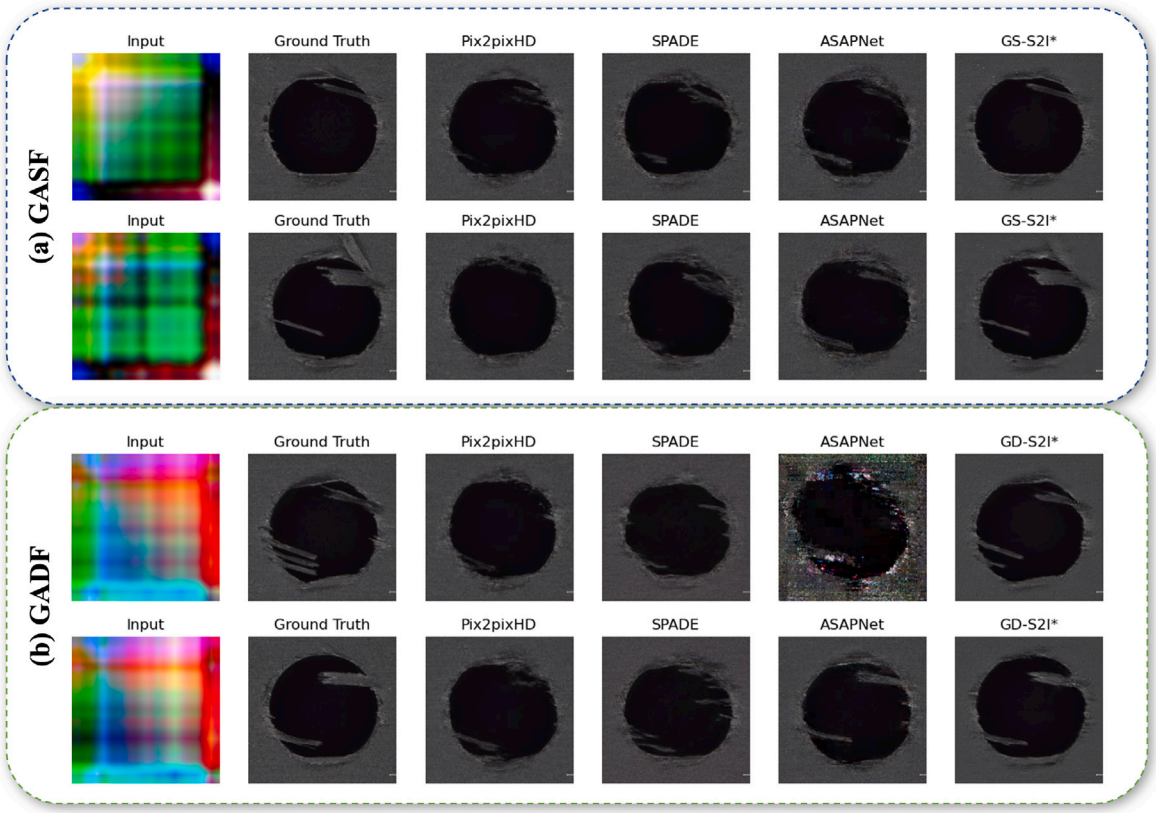

Fig. 7. Qualitative comparison of various baselines in different GAF images.

Table 4
Quality assessment score comparison of Sensor2Image and existing methods in the literature.

	GASF		GADF	
Baseline	PSNR (↑)	SSIM (↑)	PSNR (↑)	SSIM (↑)
pix2pixHD (Park et al., 2019)	22.29 ± 0.04	0.55 ± 0.0	22.32 ± 0.04	0.54 ± 0.0
SPADE (Wang et al., 2018)	21.66 ± 0.32	0.5 ± 0.01	22.03 ± 0.14	0.5 ± 0.0
ASAPNet (Shaham et al., 2021)	21.79 ± 0.04	0.51 ± 0.01	20.83 ± 0.02	0.49 ± 0.01
Proposed	**23.67 ± 0.30**	**0.60 ± 0.01**	**22.74 ± 0.07**	**0.61 ± 0.01**

force sensor data to synthesize hole surface images. This misalignment with the problem requirements contributed to the relatively inferior performance observed.

4.2. Qualitative results

Sensor2Image generated visually realistic machined surface images from the force sensors during the drilling process, as shown in Fig. 7. The top two input sets were generated using the GASF, whereas the bottom two were generated using the GADF. The proposed fine-tuned models, GS-S2I* for GASF and GD-S2I* for GADF, were employed.

A key finding of this research is that the fine-tuned models, GS-S2I* and GD-S2I*, demonstrated superior qualitative results compared with other baseline approaches. These models could more accurately capture intricate details and learn overall patterns in machined surface images. This superiority was evident regardless of the sensor-to-image generation method employed, whether GASF or GADF. GS-S2I* and GD-S2I* could generate visually realistic images without exhibiting bias towards any specific input generation method, highlighting their robustness and flexibility in handling varied data inputs. Such capabilities indicate the advanced potential of these models for rendering more precise and detailed representations of machined surfaces, marking a significant advancement over baseline methods in the field.

5. Conclusion

Sensor2Image marks a significant breakthrough in the field of CFRP drilling processes by introducing a novel approach for generating drilled-hole surface images from force sensor data. This method provides a unique visual inspection tool that facilitates comprehensive and measurement-agnostic delamination prediction and analysis. Unlike previous methods that focused on specific delamination factors, the proposed model could more comprehensively predict the extent of defects, rendering it highly suitable for practical applications.

To generate images similar to real delamination patterns and with distinct features, this work designed the loss functions of Sensor2Image for the generator and discriminator. Further, the weights of the loss terms in the total loss were experimentally adjusted. The L_1 loss was used as a regularizer in the generator's loss function to ensure similarity to real delamination patterns, whereas the LS loss function was incorporated in the discriminator to produce less blurred and clearer outputs. Moreover, the weight λ between the adversarial loss and the L_1 loss was considered as well, which determined the final loss.

The effectiveness and versatility of Sensor2Image was demonstrated through qualitative and quantitative analysis. A comparative analysis for qualitatively comparing Sensor2Image to other state-of-the-art approaches such as pix2pixHD, SPADE, and ASAPNet was performed. Sensor2Image outperformed other approaches, which, despite their

strengths in generating high-resolution images, incorporating style information, or enabling rapid image translation, were not the best choices for the task performed. Further, the qualitative results indicated that Sensor2Image produced visually realistic images of machined surfaces, thereby accurately capturing the intricate details and overall patterns.

Quantitative analysis using PSNR and SSIM metrics showed that the fine-tuned models, GS-S2I*, and GD-S2I*, achieved superior image quality compared to the original pix2pix configuration. The proposed models demonstrated outstanding performance in terms of the simultaneous prediction of multiple delamination factors, as evidenced by their low MAPE and MAE values. This ability to predict multiple factors distinguishes Sensor2Image from traditional machine learning models that focus on a single delamination factor. Moreover, the flexibility of Sensor2Image facilitates broad applicability to different situations and delamination factors.

To the best of the authors' knowledge, this marks the first attempt at generating image predictions based on sensory data. This innovative approach is particularly beneficial for processes requiring multiple delamination factors because it facilitates intuitive verification of process outcomes through visual representations. The proposed approach can enhance the efficiency and reliability of industrial processes, particularly those involving complex delamination factors. Furthermore, the visual output offers a more accessible means of monitoring and interpreting process results.

The potential areas for future research include the customization of Sensor2Image for specific applications in the aerospace and manufacturing industries. Further, its applicability can be extended to different composite materials. This would broaden its use in critical applications wherein material integrity is crucial. In addition, evaluating the effect of tool wear on delamination and incorporating it into the model could provide valuable insights. Although the experiments in this work were designed to minimize tool wear through frequent tool changes, it may be worthwhile to explore the impact of less frequent tool changes to obtain a more comprehensive understanding of the effect of tool wear on delamination. Advanced machine learning techniques that can handle variations in tool wear should be investigated to improve model robustness. The integration of data from the additional sensors that monitor the drilling process could provide valuable findings. Multisensor data fusion approaches can facilitate a more comprehensive characterization of defect formation mechanisms and offer insights into process dynamics. Leveraging these additional data streams can potentially boost the predictive performance and robustness of the proposed method for robotic drilling operations. Future research will explore the integration of various sensor data to enhance the understanding of the drilling process and improve the prediction of delamination. Moreover, although the current work did not explicitly incorporate the effect of vibration, investigating dedicated mechanisms for vibration isolation when conducting experiments can be a valuable research direction. The consideration of vibration effects can enhance process control precision and decrease the defects in vibration-prone robotic machining environments.

CRediT authorship contribution statement

Jae Gyeong Choi: Conceptualization, Data curation, Methodology, Software, Validation, Formal analysis, Investigation, Resources, Writing – original draft, Writing – review & editing, Visualization. **Dong Chan Kim:** Conceptualization, Data curation, Investigation, Resources, Writing – review & editing, Visualization. **Miyoung Chung:** Conceptualization, Data curation, Software. **Gyeongho Kim:** Validation, Formal analysis, Writing – review & editing. **Hyung Wook Park:** Writing – review & editing, Project administration, Funding acquisition. **Sunghoon Lim:** Conceptualization, Methodology, Validation, Writing – review & editing, Supervision, Project administration, Funding acquisition.

Declaration of competing interest

The authors declare that they have no known competing financial interests or personal relationships that could have appeared to influence the work reported in this paper.

Data availability

Data will be made available on request.

Acknowledgments

This work was supported by the National Research Foundation of Korea (NRF) grant funded by the Korea government (MSIT) (No. RS-2024-00335260 and No. 2022R1A6A3A13065684), Institute of Information & communications Technology Planning & Evaluation (IITP) grant funded by the Korea government (MSIT) (No. RS-2020-II201336, Artificial Intelligence Graduate School Program (UNIST)), and the Advanced Technology Center Plus (ATC+) Program (20017932, 50% Accident Prevention Focus to reduce accident rate Development of Risk Detection System for Road Facilities Based on Artificial Intelligence) funded by the Ministry of Trade, Industry and Energy (MOTIE).

References

Adachi, M., Budvytis, I., Ducati, C., & Cipolla, R. (2020). Physics-aware image-to-image translation to explore long-life all-solid-state batteries. URL: https://api.semanticscholar.org/CorpusID:231659480.

Chen, R., Li, S., Zhou, Y., Qiu, X., Li, P., Zhang, H., & Wang, Z. (2023). Damage formation and evolution mechanisms in drilling CFRP with prefabricated delamination defects: Simulation and experimentation. *Journal of Materials Research and Technology*, *26*, 6994–7011. http://dx.doi.org/10.1016/j.jmrt.2023.09.065.

Chen, Y., Zhang, D., Deng, C., & Song, Y. (2022). Integrated learning method of gramian angular field and optimal feature channel adaptive selection for bearing fault diagnosis. In *2022 8th international conference on control, automation and robotics* (pp. 209–217). http://dx.doi.org/10.1109/ICCAR55106.2022.9782625.

Choi, J. G., Kim, D. C., Chung, M., Lim, S., & Park, H. W. (2024). Multimodal 1D CNN for delamination prediction in CFRP drilling process with industrial robots. *Computers & Industrial Engineering*, *190*, Article 110074. http://dx.doi.org/10.1016/j.cie.2024.110074.

Ciecieląg, K., Skoczylas, A., Matuszak, J., Zaleski, K., & Kęcik, K. (2021). Defect detection and localization in polymer composites based on drilling force signal by recurrence analysis. *Measurement*, *186*, Article 110126. http://dx.doi.org/10.1016/j.measurement.2021.110126.

Cui, J., Liu, W., Zhang, Y., Gao, C., Lu, Z., Li, M., & Wang, F. (2021). A novel method for predicting delamination of carbon fiber reinforced plastic (CFRP) based on multi-sensor data. *Mechanical Systems and Signal Processing*, *157*, Article 107708. http://dx.doi.org/10.1016/j.ymssp.2021.107708.

Davim, J., & Reis, P. (2003). Drilling carbon fiber reinforced plastics manufactured by autoclave—experimental and statistical study. *Materials & Design*, *24*(5), 315–324. http://dx.doi.org/10.1016/s0261-3069(03)00062-1.

Déau, G., Bourdon, P., Carré, P., Mérillou, S., Dervillé, A., & Mourougaya, F. (2023). PREFAB-GEN : AD HOC image generation for pre-manufacturing of tires using image-to-image translation. In *2023 IEEE international conference on image processing* (pp. 1610–1614). http://dx.doi.org/10.1109/ICIP49359.2023.10222342.

Feito, N., López-Puente, J., Santiuste, C., & Miguélez, M. (2014). Numerical prediction of delamination in CFRP drilling. *Composite Structures*, *108*, 677–683. http://dx.doi.org/10.1016/j.compstruct.2013.10.014.

Geier, N., Patra, K., Anand, R. S., Ashworth, S., Balázs, B. Z., Lukács, T., Magyar, G., Tamás-Bényei, P., Xu, J., & Davim, J. P. (2023). A critical review on mechanical micro-drilling of glass and carbon fibre reinforced polymer (GFRP and CFRP) composites. *Composites Part B (Engineering)*, *254*, Article 110589. http://dx.doi.org/10.1016/j.compositesb.2023.110589.

Girot, F., Dau, F., & Gutiérrez-Orrantia, M. E. (2017). New analytical model for delamination of CFRP during drilling. *Journal of Materials Processing Technology*, *240*, 332–343. http://dx.doi.org/10.1016/j.jmatprotec.2016.10.007.

Huang, J., Liao, J., & Kwong, S. (2021). Semantic example guided image-to-image translation. *IEEE Transactions on Multimedia*, *23*, 1654–1665. http://dx.doi.org/10.1109/tmm.2020.3001536.

Ismail, S. O., Ojo, S. O., & Dhakal, H. N. (2017). Thermo-mechanical modelling of FRP cross-ply composite laminates drilling: Delamination damage analysis. *Composites Part B (Engineering)*, *108*, 45–52. http://dx.doi.org/10.1016/j.compositesb.2016.09.100.

Isola, P., Zhu, J.-Y., Zhou, T., & Efros, A. A. (2017). Image-to-image translation with conditional adversarial networks. In *Proceedings of the IEEE conference on computer vision and pattern recognition*.

Jiang, J.-R., & Chen, H.-C. (2023). Manufacturing quality prediction based on deep learning in conjunction with gramian angular and Markov transition fields. In *2023 international conference on consumer electronics - Taiwan* (pp. 439–440). http://dx.doi.org/10.1109/ICCE-Taiwan58799.2023.10226930.

Kim, G., Yang, S. M., Kim, D. M., Kim, S., Choi, J. G., Ku, M., Lim, S., & Park, H. W. (2023a). Bayesian-based uncertainty-aware tool-wear prediction model in end-milling process of titanium alloy. *Applied Soft Computing*, *148*, Article 110922. http://dx.doi.org/10.1016/j.asoc.2023.110922.

Kim, G., Yang, S. M., Kim, S., Kim, D. Y., Choi, J. G., Park, H. W., & Lim, S. (2023b). A multi-domain mixture density network for tool wear prediction under multiple machining conditions. *International Journal of Production Research*, 1–20. http://dx.doi.org/10.1080/00207543.2023.2289076.

Krishnamoorthy, A., Mercy, L., Vineeth, K., & Kumar, M. (2015). Delamination analysis of carbon fiber reinforced plastic (CFRP) composite plates by thermo graphic technique. *Materials Today: Proceedings*, *2*, 3132–3139. http://dx.doi.org/10.1016/j.matpr.2015.07.101.

Li, G., Ao, J., Hu, J., Hu, D., Liu, Y., & Huang, Z. (2024). Dual-source gramian angular field method and its application on fault diagnosis of drilling pump fluid end. *Expert Systems with Applications*, *237*, Article 121521. http://dx.doi.org/10.1016/j.eswa.2023.121521.

Liu, D., Cheng, W., & Wen, W. (2020). Rolling bearing fault diagnosis via STFT and improved instantaneous frequency estimation method. *Procedia Manufacturing*, *49*, 166–172. http://dx.doi.org/10.1016/j.promfg.2020.07.014.

Mao, X., Li, Q., Xie, H., Lau, R. Y., Wang, Z., & Paul Smolley, S. (2017). Least squares generative adversarial networks. In *Proceedings of the IEEE international conference on computer vision*.

Nadir, F., Elias, H., & Messaoud, B. (2020). Diagnosis of defects by principal component analysis of a gas turbine. *SN Applied Sciences*, *2*(5), http://dx.doi.org/10.1007/s42452-020-2796-y.

Norcahyo, R., Soepangkat, B. O. P., & Effendi, M. K. (2019). Minimization of the hole entry and hole exit delamination on drilling process of carbon fiber reinforced polymer using BPNN-PSO. *AIP Conference Proceedings*, *2114*(1), Article 060005. http://dx.doi.org/10.1063/1.5112476.

Ozkan, D., Gok, M. S., & Karaoglanli, A. C. (2020). Carbon fiber reinforced polymer (CFRP) composite materials, their characteristic properties, Industrial Application Areas and their machinability. (pp. 235–253). ISBN: 978-3-030-39061-7, http://dx.doi.org/10.1007/978-3-030-39062-4_20.

Park, T., Liu, M.-Y., Wang, T.-C., & Zhu, J.-Y. (2019). Gaugan: semantic image synthesis with spatially adaptive normalization. In *ACM SIGGRAPH 2019 real-time live!*. New York, NY, USA: Association for Computing Machinery, http://dx.doi.org/10.1145/3306305.3332370.

Patro, S., & Sahu, K. K. (2015). Normalization: A preprocessing stage. arXiv preprint arXiv:1503.06462.

Pérez-Salinas, C., Castro-Miniguano, C., Moya-Moya, E., & Goyos, L. (2023). Analysis of surface roughness and delamination factor applied to the drilling of hybrid polymeric composite materials by the taguchi method. *Materials Today: Proceedings*, http://dx.doi.org/10.1016/j.matpr.2023.06.437.

Sen, S., Husom, E. J., Goknil, A., Politaki, D., Tverdal, S., Nguyen, P., & Jourdan, N. (2023). Virtual sensors for erroneous data repair in manufacturing a machine learning pipeline. *Computers in Industry*, *149*, Article 103917. http://dx.doi.org/10.1016/j.compind.2023.103917.

Seo, J., Kim, Y., Kim, D. C., & Park, H. W. (2021). Numerical and experimental investigation of the delamination in drilling of the carbon fiber-reinforced plastic composite. *International Journal of Advanced Manufacturing Technology*, *112*(7–8), 2373–2387. http://dx.doi.org/10.1007/s00170-020-06452-x.

Shaham, T. R., Gharbi, M., Zhang, R., Shechtman, E., & Michaeli, T. (2021). Spatially-adaptive pixelwise networks for fast image translation. In *Proceedings of the IEEE/CVF conference on computer vision and pattern recognition*.

Su, F., Zheng, L., Sun, F., Deng, Z., & Qiu, X. (2019). Theoretical modeling for the exit-delamination morphology of the unidirectional CFRPs. *International Journal of Advanced Manufacturing Technology*, *102*, 533–544.

Sugita, N., Shu, L., Kimura, K., Arai, G., & Arai, K. (2019). Dedicated drill design for reduction in burr and delamination during the drilling of composite materials. *CIRP Annals*, *68*, http://dx.doi.org/10.1016/j.cirp.2019.04.094.

Sun, L., Hu, S. J., & Freiheit, T. (2021). Feature-based quality classification for ultrasonic welding of carbon fiber reinforced polymer through Bayesian regularized neural network. *Journal of Manufacturing Systems*, *58*, 335–347. http://dx.doi.org/10.1016/j.jmsy.2020.12.016.

Volety, R., & Mani, G. (2023). AI-based predictive modeling of delamination factor for carbon fiber-reinforced polymer (CFRP) drilling process. *Optimization Techniques in Engineering: Advances and Applications*, 139–153.

Wang, Z., Bovik, A., Sheikh, H., & Simoncelli, E. (2004). Image quality assessment: From error visibility to structural similarity. *IEEE Transactions on Image Processing*, *13*(4), 600–612. http://dx.doi.org/10.1109/tip.2003.819861.

Wang, J., Li, S., Ji, W., Jiang, T., & Song, B. (2022). A T-CNN time series classification method based on gram matrix. *Scientific Reports*, *12*(1), http://dx.doi.org/10.1038/s41598-022-19758-5.

Wang, T.-C., Liu, M.-Y., Zhu, J.-Y., Tao, A., Kautz, J., & Catanzaro, B. (2018). High-resolution image synthesis and semantic manipulation with conditional GANs. In *Proceedings of the IEEE conference on computer vision and pattern recognition*.

Wang, Z., & Oates, T. (2015). Imaging time-series to improve classification and imputation. arXiv preprint arXiv:1506.00327.

Wang, H., Sun, W., Sun, W., Ren, Y., Zhou, Y., Qian, Q., & Kumar, A. (2023). A novel tool condition monitoring based on gramian angular field and comparative learning. *International Journal of Hydromechatronics*, *6*(2), 93. http://dx.doi.org/10.1504/ijhm.2023.130510.

Xu, J., Geier, N., Shen, J., Krishnaraj, V., & Samsudeensadham, S. (2023). A review on CFRP drilling: fundamental mechanisms, damage issues, and approaches toward high-quality drilling. *Journal of Materials Research and Technology*, *24*, 9677–9707. http://dx.doi.org/10.1016/j.jmrt.2023.05.023.

Yi, Q., Tian, G., Malekmohammadi, H., Zhu, J., Laureti, S., & Ricci, M. (2019). New features for delamination depth evaluation in carbon fiber reinforced plastic materials using eddy current pulse-compression thermography. *NDT & E International*, *102*, 264–273. http://dx.doi.org/10.1016/j.ndteint.2018.12.010.

Zhang, Y., & Xu, X. (2020). Predicting the delamination factor in carbon fibre reinforced plastic composites during drilling through the Gaussian process regression. *Journal of Composite Materials*, *55*(15), 2061–2068. http://dx.doi.org/10.1177/0021998320984245.